

Persistent fluid flows defined by active matter boundaries

Zijie Qu ^{1✉}, Dominik Schildknecht ^{1✉}, Shahriar Shadkhoo ¹, Enrique Amaya¹, Jialong Jiang¹, Heun Jin Lee², David Larios¹, Fan Yang ¹, Rob Phillips^{1,2,3} & Matt Thomson ^{1✉}

Biological systems control ambient fluids through the self-organization of active protein structures, including flagella, cilia, and cytoskeletal networks. Self-organization of protein components enables the control and modulation of fluid flow fields on micron scales, however, the physical principles underlying the organization and control of active-matter-driven fluid flows are poorly understood. Here, we use an optically-controlled active-matter system composed of microtubule filaments and light-switchable kinesin motor proteins to analyze the emergence of persistent flow fields. Using light, we form contractile microtubule networks of varying size and shape, and demonstrate that the geometry of microtubule flux at the corners of contracting microtubule networks predicts the architecture of fluid flow fields across network geometries through a simple point force model. Our work provides a foundation for programming microscopic fluid flows with controllable active matter and could enable the engineering of versatile and dynamic microfluidic devices.

¹Division of Biology and Biological Engineering, California Institute of Technology, Pasadena, CA, USA. ²Department of Applied Physics, California Institute of Technology, Pasadena, CA, USA. ³Department of Physics, California Institute of Technology, Pasadena, CA, USA. ✉email: zijiequ@caltech.edu; dominik.schildknecht@gmail.com; mthomson@caltech.edu

Control of fluids is essential for biological processes, including motility and material transport across the cell, tissue, and organismal scales of organization^{1–6}. For example, within cells, cytoskeletal networks composed of filaments and motor proteins induce cytoplasmic flows or streams that drive processes ranging from chloroplast transport in algae to the recycling of motility proteins during eukaryotic chemotaxis^{1,7,8}. The key conceptual challenge is to understand how self-organized “active” protein structures like cilia and cytoskeletal networks convert chemical energy into mechanical forces at molecular scales to generate and modulate fluid flow fields on micron length scales. Here, active structures refer to systems consuming chemical energy to generate forces through self-organization. In contrast to such systems, in a conventional systems like a pipe or propeller, fluid flows emerge due to the macroscopic forces applied to boundary conditions^{9–11}. However, in cellular flow control, force fields emerge from within the fluid itself through the action and molecular self-organization of motor and filament proteins. Protein components both induce and respond to fluid flows, so that flows alter the distribution of force and material over time.

Simplified active matter systems allow the analysis of self-organized fluid control as well as providing a potential platform for technology development. Active matter systems composed of purified filament and motor proteins can generate nonequilibrium, self-organized structures, including microtubule asters,^{12–14} that generate spontaneous fluid flows^{10,15–18}. However, these fluid flows are typically disorganized and chaotic. Artificial boundaries can be applied to confine active systems experimentally and organize fluid flows by imposing boundary conditions¹⁰. Recently, we developed an optically controlled active matter system¹⁹ (Fig. 1a) composed of microtubules and engineered kinesin motor proteins, where fluid flows can be generated and modulated with light, with organized fluid flows emerging through optically guided self-organization of microtubules and motors into networks that induce flow in ambient fluids. However, while we can demonstrate that the geometry of the light inputs into the system alters patterns of fluid flow, we lack a predictive understanding of how flow fields become spontaneously self-organized through active matter dynamics.

In this paper, we apply our light-switchable active matter system to analyze the emergence of self-organized flow fields within optically-controlled active matter. We generate microtubule networks of different sizes and shapes that induce persistent fluid flows. By using light to modulate the geometry of microtubule-motor networks, we demonstrate that self-organized flow fields emerge through dynamic feedback between microtubule network contraction and fluid-driven mass transport. Fluid-network interactions generate persistent microtubule flux at the corners of contracting, polygonal microtubule networks. The geometry of microtubule flux at the network boundary predicts the steady-state flow field for a wide range of polygonal microtubule network geometries. We develop a simple theoretical model based upon boundary point forces that predicts the qualitative and quantitative flow fields generated by polygonal microtubule network contraction. The boundary force model provides a formal and integrated framework for predicting flow fields and allows quantitative comparison with experimental data, thus extending prior work¹⁹. Our boundary force model reveals that the flow field generated by microtubule networks spanning hundreds of microns can be understood as the flow field generated by simple point-force solutions of Stokes equation where point forces pointing towards the center, scaling in amplitude with the distance to the center, are arranged on the corners of a contracting microtubule network. Our results reveal a dynamic mechanism of fluid flow generation in active microtubule

networks and provide a modeling framework to predict the flow-field architecture from an active matter-generated boundary condition.

Results

Microtubule network contraction induces mass transport and persistent fluid flows. Our active matter system consists of stabilized microtubule filaments and kinesin motor proteins which, when modulated by light, induce fluid flow (Fig. 1a; Methods). The engineered kinesin motor protein reversibly cross-link under illumination (Fig. 1a) inducing interactions between motors on neighboring microtubules leading to microtubule network formation, contraction, and the generation of persistent fluid flows. In previous work¹⁹, we described the emergence of active-matter-driven fluid flows within the experimental system. However, the mechanism of flow generation and modulation has remained poorly understood and quantitative comparisons between theory and experiment have not been previously reported.

We developed an experimental platform¹⁹ that allows us to optically induce and track both microtubule and flow-field dynamics (Supplementary Methods 2). Our experimental system (Fig. 1b) uses a conventional fluorescence microscope and a digital light projector to control sample illumination. We tracked microtubule dynamics via a fluorescent microtubule dye and, simultaneously, introduced micron-sized tracer particles to quantify the flow-field architecture through particle tracking. The experimental system allows us to induce microtubule networks of differing sizes and shape with light and to track the dynamics of the active matter-fluid system as the fluid flows emerge.

We analyzed the fluid and microtubule dynamics induced by optical activation of a 600 μm square region (Fig. 1c–e, Supplementary Methods 3 and 4). Light activation-induced persistent fluid flows through the formation of a microtubule network that spontaneously contracted to its center of mass. As the microtubule network contracted, it induced fluid flows within the bulk microtubules (Fig. 1d, cyan arrows) outside of the light-activated region, as quantified by particle image velocimetry (PIV) (Supplementary Fig. 1). The background flows lead to an influx of microtubules along the corners of the contracting microtubule network leading to an increase in integrated microtubule density within the illuminated region over time (Supplementary Fig. 2, Supplementary Note 1). Persistent microtubule flux at the network corners was maintained for more than 15 min due to a persistent influx of microtubules from the background solution into the light-activated region (Supplementary Movie 1). We observed similar microtubule flux in simulations of contracting square microtubule networks (Methods). In these simulations, we treated each position within a contracting microtubule network as a point force whose amplitude is set by the contractile velocity of the network^{20,21}. Each point force acts as a source for fluid flow due to Stokesian fluid dynamics^{22,23} (Fig. 1f, g). In these simulations, microtubule network contractions generated a fluid flow field that leads to inflows of even more particles at the network corners.

Experimentally, the emergence of persistent microtubule flux at the corners of the contracting network coincides with the emergence of steady-state fluid inflows (Fig. 1h) along the corners of the square and fluid outflows along the edges of the activation region. In addition, the fluid flow field contains four pairs of approximately 100 μm (in radius) centers of vorticity oriented along each arm of the microtubule structure. Broadly, fluid inflows align with the persistent influx of microtubules along the microtubule network corners. The observation is consistent with a model where microtubule influx along the corners of the network act as force sources that generate the fluid flows.

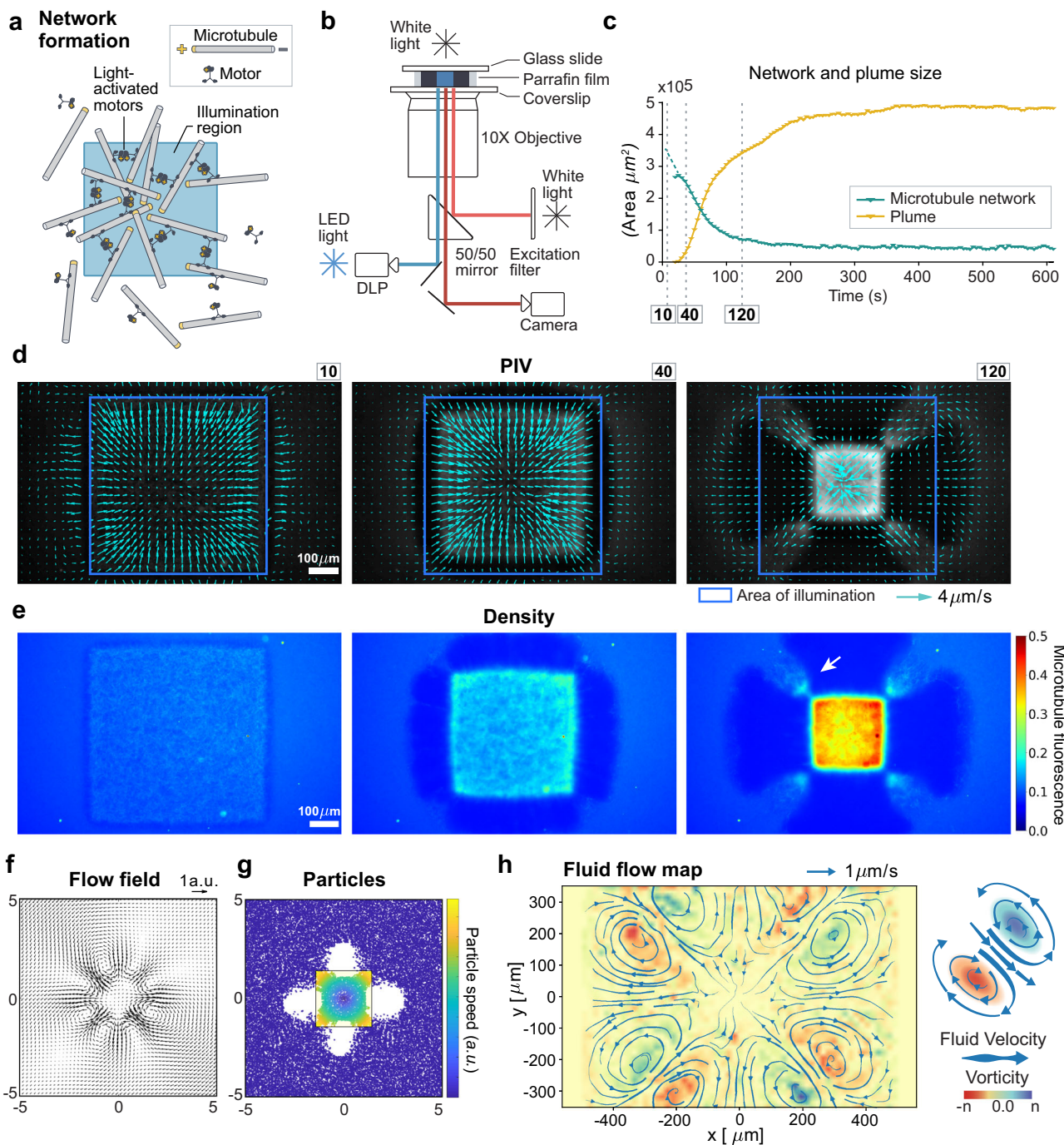


Fig. 1 Constant illumination of the active matter system leads to microtubule network contraction and persistent fluid flows. **a** The active matter system used in this study consists of fluorescently labeled, stabilized microtubule filaments and kinesin motors that cross-link under illumination. **b** The experimental setup: the microtubules are visualized with a fluorescence microscope; the cross-linking of the motors is controlled temporally and spatially by projecting light patterns using a digital light projector, the inert tracer particles are visualized with white light for measuring fluid flow. **c** The network and plume sizes as a function of time measured by image analysis for the time series shown in **(d)** with three snapshots of the contracting network at $t = 10, 40,$ and 120 s (Supplementary Methods 5). The snapshots show the contracting network with the emergence of arm-like microtubule bundles by projecting a $600 \mu\text{m}$ square pattern (depicted in blue); the cyan arrows demonstrate the steady-state fluid flow caused by the active force of the network; the scale bar is $100 \mu\text{m}$. **e** Snapshots at the same time with overlaid microtubule density as extracted from image analysis where the white arrow indicates the position of a microtubule arm. **f, g.** Microtubule flux emerges at the network corners in a particle simulation where each particle is modeled as a point force. In particular, **f** shows the resulting fluid flow and **g** the particle distribution with color indicating particle velocity. **h** Time-averaged flow field showing a persistent structure: four inflows along the diagonal of the projected square pattern, four outflows perpendicular to the edges, and eight vortices. It is illustrated in the schematic that the vortices are located at both sides of the inflows. It should be noted that microtubule accumulation is much quicker than the velocity experiments shown in **(f)**, and hence can be neglected in the description.

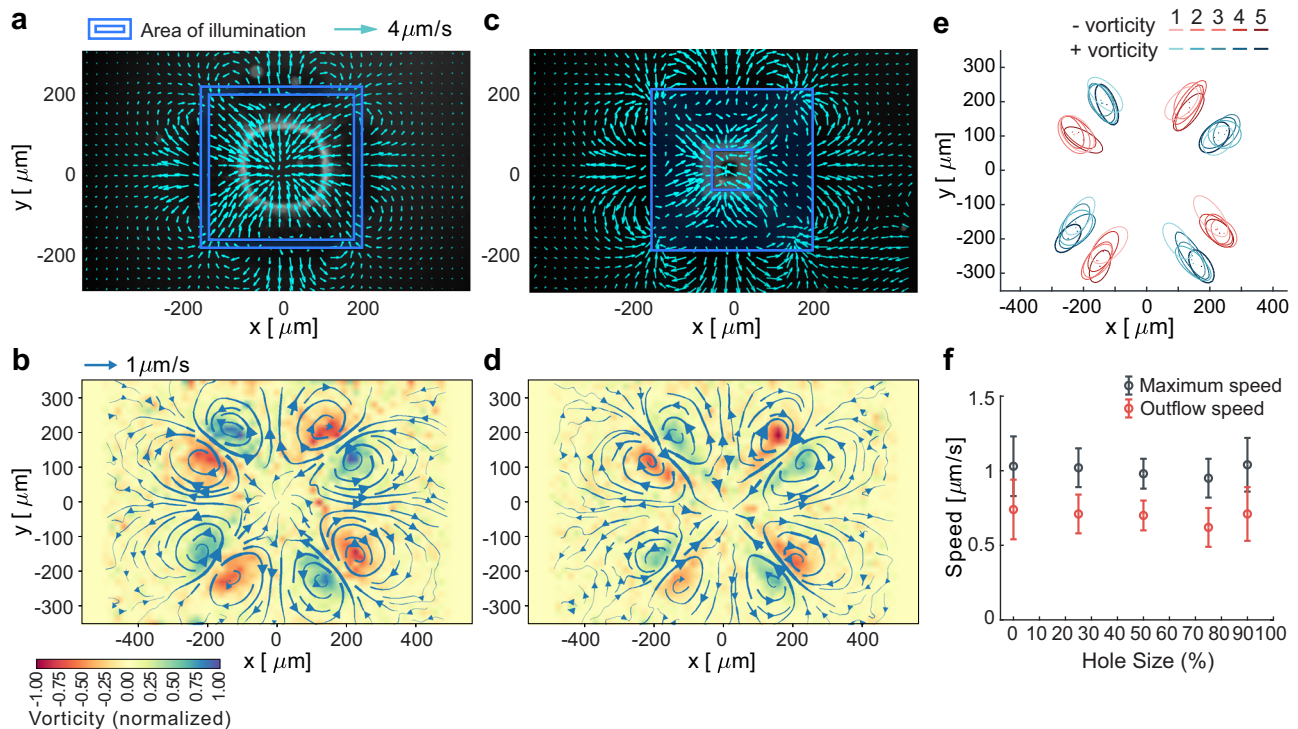


Fig. 2 Experimental fluid flow for square illumination patterns is not affected by introducing a cavity at the network center. **a, c** The projected light patterns are hollow squares (400 μm in length, 100 s after the first illumination) with different cavity sizes; (**a** the cavity spans 90% of the square's size, **c** the cavity spans 25% of the square's size). **b, d** Time-averaged flow fields depicted with blue streamlines, corresponding to illuminations depicted in panels (**a, c**) (more cases in Supplementary Fig. 4); the initial contracting network demonstrates different behavior, yet the microtubule fluxes are the same as demonstrated by the PIV result; the resulting flow fields are persistent and show similar flow fields—four inflow along the diagonal directions and outflow from the edges, plus eight vortices. **e** The vorticity peaks and valleys from different hollow square experiments overlap. The numbers 1–5 correspond to cavities spanning 0%, 90%, 75%, 50% and 25% of the square's size. **f** The maximum inflow and outflow velocities are similar across all experiments, the data are averaged over five individual experiments, each experiment has four maximum inflow and outflow values; the error bar shows the standard deviation.

Microtubule network boundary geometry determines the organization of the flow field. We found that the geometry of the microtubule network boundary alone is sufficient to determine the architecture of the microtubule influx as well and the fluid flow fields for square microtubule networks. To analyze the role of the microtubule flux along the boundary of the microtubule network in generating and organizing fluid flows, we created a series of 400 μm microtubule networks with a square boundary where we introduced square cavities into the center of the network (Fig. 2a–d, Supplementary Figs. 2 and 3, Supplementary Note 2). In total, we created four different networks with cavities ranging from 100 to 360 μm (25% and 90%) in length. By altering the distribution of active material and the network topology, the hollow networks allowed us to examine the relative contribution of the network boundary and interior to the generation of the fluid flow field.

The hollow square networks execute a similar process of microtubule network formation, network contraction, and boundary linking, leading to persistent microtubule flux at network corners. For the hollow shapes, the contractile network adopts the geometry of the light pattern, so that network itself contains a square hole throughout the network contraction (Fig. 2a). In each case, the contracting network generates a diagonal distribution of microtubule flux at the corners of the illumination region (Fig. 2a, c, Supplementary Figs. 3 and 4). The microtubule distribution observed for the hollow networks is qualitatively similar to the material distribution generated by the

contraction of the intact square network. Like the intact square network in Fig. 1d, the hollow networks generate a persistent microtubules influx in the form of arms along the network corners (Supplementary Movies 2–5).

The hollow squares also generate persistent fluid flow fields (Fig. 2b, d) that are very similar to the intact square networks in terms of their qualitative and quantitative features. Like the filled square network, hollow-network-induced fluid flow fields exhibited diagonal inflows, edge outflows, and a series of vortex pairs. The vortex pairs across all networks were quantitatively comparable in their size and location (Fig. 2e). We quantified the position of vortices by fitting the vorticity ($\nabla \times \mathbf{v}$) with a Gaussian mixture model and extracting the centroid and shape of each vorticity peak or valley. The extracted vorticity peaks across the five different networks had centroid centers lying within 10 μm of one another (Fig. 2e). Further, the maximum of the fluid velocity was approximately $1 \mu\text{m s}^{-1}$ along the inflow and $0.7 \mu\text{m s}^{-1}$ along the outflow (Fig. 2f), and the maximal and minimal fluid speeds agree across the five networks to within the variation measured for replicates of individual networks.

The distribution of microtubule density and flux at the corners of the applied light pattern was similar for the four cavity networks and the full square network. This finding suggests that the microtubule flux at the corners of the contracting networks plays a central role in determining the architecture of the generated fluid flows. In addition, supporting the notion of the flow being driven by the microtubule flux, circular light patterns

generate networks that exhibit radial contraction without persistent fluid flow or microtubule arms (Supplementary Fig. 5, Supplementary Note 3).

The boundary force model predicts flow-field geometry. Based on our analysis of the flow fields induced by the hollow square networks, we developed a simple mathematical model to predict the architecture of fluid flow fields generated by contracting microtubule networks using boundary forces alone. The boundary force model formalizes and extends previous work¹⁹ in which we proposed a qualitative model for fluid flows by placing Stokeslets at all locations within a contracting microtubule network. In our boundary force model, the microtubule influx at the corners of the network generates the force that is transferred to the fluid to induce flow. Our model is based upon the following observations. First, microtubule network contraction leads to diagonal inflows of activated microtubules at the corners of the contracting microtubule network. Second, networks with a square boundary but distinctly different internal structures induce nearly identical patterns of fluid flow. Third, moving microtubules are known to act on their ambient fluid as local point sources of force. Therefore, we propose that the force generated by active microtubule flux along the corners of the contracting network determines the architecture of the induced flow field. In what follows we develop the boundary force model, and then demonstrate that the model allows flow field predictions that can be compared quantitatively with experimental data. In addition to enabling quantitative comparison the boundary force model provides insight into how key features of the flow fields, including the position of vortices, are determined by active matter network geometry.

In our boundary force model, the fluid is considered in the incompressible Stokesian limit (valid at low Reynolds numbers) so that the fluid velocity \mathbf{v} obeys the Stokes equation

$$\mu \nabla^2 \mathbf{v} - \nabla p + \mathbf{f} = 0, \quad \nabla \cdot \mathbf{v} = 0, \quad (1)$$

where μ is the fluid viscosity, p is the pressure, and \mathbf{f} is the force field exerted by the active matter. The hypothesis is that for convex polygonal illumination patterns the geometry of the corners determines the flow. In this model, it means \mathbf{f} to be non-vanishing only in the corners. Therefore, \mathbf{f} is a sum of four-point forces directed toward the center of the shape for a rectangular pattern illumination, due to symmetry. These properties determine Eq. (1) up to a trivial rescaling of all quantities since Eq. (1) is linear.

Due to the linearity of Eq. (1), the fundamental solution could be used to obtain the flow field for free boundary conditions²⁴. However, incorporating more general boundary conditions in this solution method can be challenging²⁵. In this particular case, two sets of boundary conditions have to be imposed. The first set models the no-slip condition at the limits of our fluid flow cell, while the second set describes the inhibition of fluid flow due to the jamming of microtubules. This latter boundary condition is achieved by imposing an area with no slip at its boundary at the center of the activated area, with the same shape as the activation area, but with half of the (linear) dimensions. Since these boundary conditions are difficult to treat with the fundamental solution, finite-element methods (FEM) simulations were used, based on FEniCS²⁶. It should be noted that due to the limitations of FEM, point forces are spread out over a finite kernel (see Supplementary Methods 6).

Boundary force model captures aspect-ratio induced flow-field transitions for rectangular networks. For square networks, we found that the model predicted a flow field with fluid inflows

along the network diagonal and outflows along the edges leading to pairs of vortices along the corners of the networks (Fig. 3a–d, top row). In general, there is a close resemblance between the qualitative features of the experiment and theory.

We, therefore, generalized our model to predict the flow generated by rectangular networks with a range of different aspect ratios. For rectangular networks, the model predicted the correct number and position of fluid vortices (Fig. 3c). In the rectangular geometries, we experimentally observe a crossover from inflow to outflow along the long axis of the rectangle for increasing aspect ratio. Moreover, the emergence of new vortices left and right of the activated area can be well observed in the streamlines for both the experiment and theory. It is even more apparent in the vorticity, shown in the background of the figures, demonstrating the resemblance between theory and experiment.

The vorticity was further analyzed by comparing the experiment to the theory directly by fitting with a mixture of Gaussians. Comparison of their centers and their extent revealed a significant overlap between experimental and simulated centers of vorticity (Fig. 3d), with the average distance between experimental data and simulation being approximately 46 μm , which is much smaller than the typical extent of the activated region of 400 μm .

On an intuitive level, the simulated flow field can be understood as emerging from two-dimensional Stokeslets placed only at the corners of the network. Therefore, the vortices that arise at the corner of the network can be understood as emerging due to the vortex pair around the fundamental Stokeslet solution to Stokes equation for a point force²⁷. This intuitive picture can be used to address the qualitative disagreement between theory and experiment, where the peaks of vorticity do not align with the center of circulation in the simulation results, but they do in the experiment. In the simulation, the forces were (almost) point-like so that the vorticity is concentrated along the point force, as expected for Stokeslets. In contrast, in the experiment, the forces are spread out over the width of the “arm” linking the background fluid to the contractile network. The finite extent of this arm pushes the vorticity peaks apart, making them align with the center of circulation.

Finally, while the number of vortex cores and their location was our primary method of comparing the simulation results with the experiment, the fluid velocities could also be compared directly. We chose to compare along the long axis of the rectangle because the fluid velocity exhibits a (distance-dependent) crossover behavior from inflow to outflow for increasing aspect ratio. Qualitatively, we show that this crossover is seen in both experiment and simulation (Fig. 3e–g). However, a direct comparison should be viewed with caution, because the details of the crossover, such as the location of the inversion point at a fixed aspect ratio, depend on details of the simulation, such as the size of the inner jamming region, and are difficult to locate precisely in the experiment.

The boundary force description predicts flow field induced by polygonal networks. While the rectangular activation area provides a useful test case for the model, we wanted to develop a more general framework able to predict the flow fields generated by a range of polygonal shapes. In analogy, we introduced point forces on the corners of the polygonal light pattern (Supplementary Fig. 6). In each case, we found that the corner force description was sufficient to determine the number and location of fluid vortices as well as the orientation of fluid flows.

Regular triangles and hexagons were considered (Fig. 4a): Due to symmetry, forces are in the corners, pointing towards the center, and each force amplitude is the same (Supplementary Movies 6–8). An excellent qualitative agreement between theory

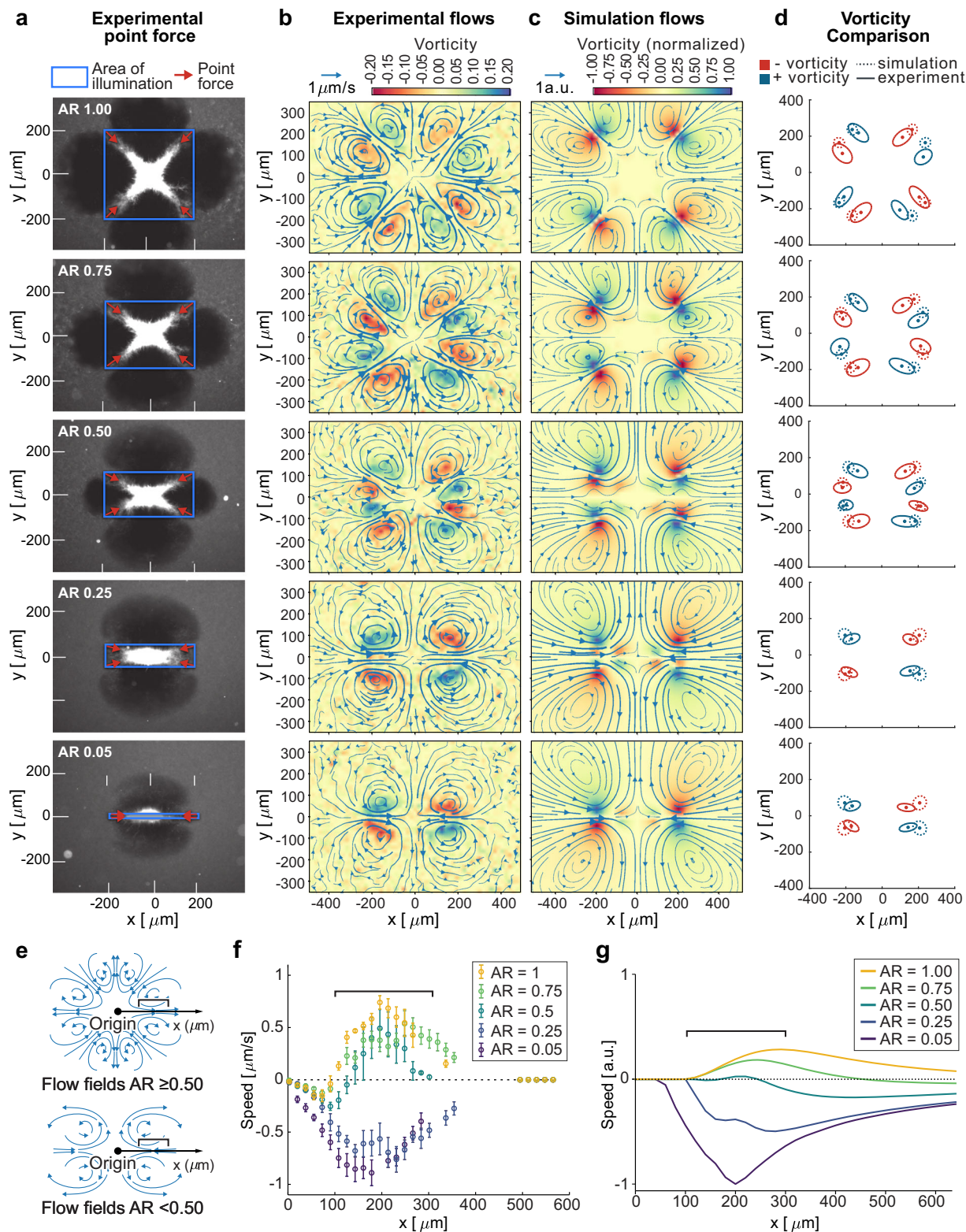


Fig. 3 The fluid flow fields agree qualitatively and quantitatively with the predictions from the boundary force model. **a** Microscopy snapshot from the experiments where the white part is the contracting network, the black region is the plume and the gray area in the background. In addition, we show the projected light patterns with a blue rectangle, the length of the rectangular pattern is $400 \mu\text{m}$ and the aspect ratios (AR) are 1 , $\frac{3}{4}$, $\frac{1}{2}$, $\frac{1}{4}$, and $\frac{1}{20}$ from top to the bottom; the red arrows indicate the locations of the point force used in the simulation. **b** Resultant time-averaged flow fields, where the blue streamlines indicate flow (velocity). **c** Simulated flow fields with a finite element method using point forces as a source term. **d** The peaks and valleys of the vorticity from experimental and simulation results show a good agreement. **e** A schematic showing the location where the velocity is measured and compared, defining the black bracket visible in (**f**, **g**) for easier comparison. **f** The horizontal component of the fluid velocity measured experimentally along the x -axis, each data point is averaged over ten individual experiments. Error bars denote one standard deviation. **g** The horizontal component of the fluid velocity measured from simulation result along the x -axis, a similar trend is observed compared to the experimental results in (**f**).

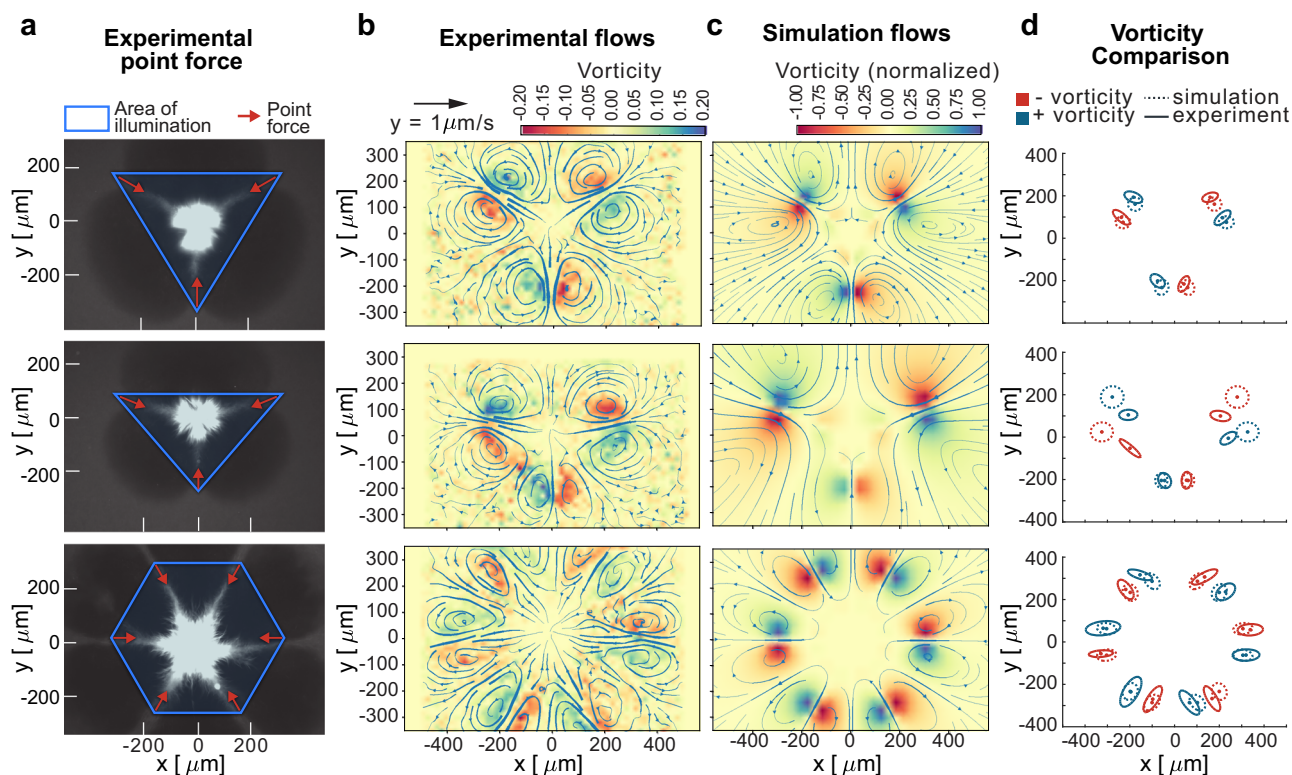


Fig. 4 The simulations can be successfully generalized to other polygonal shapes, such as triangles and hexagons. **a** Snapshot images from the experiment showing the projected pattern (illustrated by light blue), an equal-angle triangle (600 μm in length), an isosceles triangle (600 μm in width, 300 μm in height), a hexagon (600 μm from top to the bottom), the red arrows indicate the locations of the point force used in the simulation. **b** Time-averaged flow fields measured experimentally. **c** Simulated flow fields using point forces as source terms. In both **b, c**, the blue streamlines indicate the flow field. **d** The peaks and valleys of the vorticity from experimental and simulation results show a good agreement.

and experiment was observed as seen in the Gaussian mixture model comparison (Fig. 4b–d). The locations of the vorticity peaks and valleys overlap well between the experimental observation and the simulation. Hence, these comparisons demonstrate that our model can generalize to regular polygons. It should be noted that even circular activation patterns can be understood in this manner, by considering them as regular polygons with a large number of corners. Our model indeed correctly predicts the absence of flow even in this case (Supplementary Fig. 7, Supplementary Note 4).

A non-regular polygon was also considered, through an isosceles triangle (Supplementary Movie 8). Because the polygon is no longer regular, there is no longer a symmetry reason for all forces to be equally strong. While we still assume that the forces point towards the center of the activated area, we hypothesized that their amplitudes scaled linearly with distance to the center. In other words, corners farther away from the center induce a stronger fluid flow, based on published experimental results^{19,20}. It should be noted that one could additionally hypothesize a force scaling dependent on the corner angle, having the largest forces for angles closer to 0° and vanishing for 180° . However, for this paper we decided to use exclusively the simpler distance scaling, since a good agreement can be observed between the experiment and the model, therefore, providing compelling evidence that our description can also be applied to non-regular polygons (Fig. 4a–d, middle row).

Discussion

In this work, we analyze the emergence of self-organized fluid flows in an optically controlled microtubule-motor active matter system in vitro where the geometry of the active matter-induced

flow field can be modulated by an applied light pattern. We demonstrate that active-matter–fluid interactions lead to a self-organized flux of microtubules along the corners of polygonal microtubule networks. By modeling these fluxes as point forces, we are able to predict the architecture of persistent flow fields generated by a range of polygonal network geometries. Our model shows that the distribution of forces on the boundary of an active structure is sufficient to predict the flow field generated by the active matter system. The corner force field itself emerges through a self-organization process driven by microtubule network contraction and mass transport. Therefore, our model reveals how self-organized microtubule flux can control the geometry of active matter-driven fluid flows.

In our model, microtubule flux along the boundary of the active matter system plays an essential role in determining the induced flow field. The persistent, steady-state flow structure observed in this work reveals the role of force and material localization in active-matter-driven fluid flows. Our experimental system spontaneously generates organized flow fields that resemble extensional fluid flow fields²⁸. Compared with the previous model we proposed to predict the flow field generated by the same system¹⁹, the current model describes the flow architecture more accurately and through a simplified physical mechanism that only involves the network boundary. Indeed, the emergence and location of the vortices in the experiments are only correctly predicted by our model, mainly as a result of our ability to incorporate physically accurate boundary conditions. Solving the Stokes equation directly, as opposed to working with Stokeslet superpositions, enables us to explore the fundamental principles of the flow field induced by the active matter–fluid interaction. We can understand vortices as arising due to the

vortex pairs that emerge around the fundamental point-force solution to Stokes equation²⁷. The experiments with hollow squares confirm the hypothesis that the corners of the optically defined boundary determine the flow architecture, and the forces can be reduced to a single localized force in the corner in contrast to a series of forces along the diagonal. It should be noted, that our model describes the steady-state flow field well, but does not describe the transient dynamics of the system. It will be very interesting for future work to analyze the coupled active matter–fluid dynamics, which could reveal an interesting force scaling with the distance from the centroid, the corner angles, and curvature radii²⁹.

Previous work on active-matter-driven fluid flows has observed that active nematics composed of microtubules and motor proteins generate spontaneous but chaotic fluid flows fields^{15,16}. Furthermore, in these systems, confinement of the nematic within passive fabricated boundary leads to the organization of chaotic flows^{1,17}. In our system, the self-organization of microtubule density within the active matter fluid system itself generates organized flow fields. The boundary forces used in our predictive model emerge experimentally through the self-organization of microtubule “arms” at the corners of our applied light pattern. Therefore, our work reveals a mechanism of self-organized flow modulation and demonstrates how organized flows can emerge in the active matter without passive, fabricated boundaries. Indeed, cells and microorganisms use both physical and chemical mechanisms to control the shape of active matter networks to modulate fluid flows^{22,30}.

We explored a limited set of flow patterns generated by convex, polygonal network geometries. It will be important, in future work, to explore the range of fluid fields that can be generated by exploring a wider range of geometries, considering possible history dependence, and combining flow fields generated by different illumination patterns with superposition. Further, the organized flow field is a potential platform for building micro-machines. For example, it has been shown that microscopic gears can be driven by bacterial suspensions to collect mechanical energy^{31,32}, and a similar device could be combined with the microtubule–kinesin system and driven by the fluid flow as an active switch.

Methods

The active matter system consists of stabilized microtubules, kinesin motors (constructed with the light-induced hetero-dimer system), and a necessary energy mix. We note that, in our system, kinesin motor linking leads to contractile microtubule network dynamics^{19,20}. In contrast, in a related system with a depletion agent (PEG)¹⁵, the motor–microtubule system generates extensile dynamics^{15,33}.

All ingredients and buffer preparation protocols are documented in a previous paper from our group¹⁹ and we follow the exact same procedure in this study using the aster assay. Inert particles with a 1 μm diameter are suspended in the system for flow field measurement purposes. The sample chambers are made by sandwiching pre-cut Parafilm M by coated slides and coverslips^{19,34}. The measured depth of the chamber is approximately 70 μm .

The experiment is conducted on a conventional microscope (Nikon TE2000) with tenfold magnification. We customize the system by adding a programmable digital light projector (EKB Technologies DLP LightCrafter E4500 MKII Fiber Couple), which is used to activate the kinesin motors with the projected polygonal patterns. The digital light projector chip is illuminated by the 470 nm LED (ThorLabs M470L3) to project polygonal patterns and activate the cross-linking between motors. The fluorescently labeled microtubules are illuminated by 660 nm light and imaged with a digital camera (FLiR BFLY-U3-23S6M-C). The system is controlled with the Micro-Manager software package (<https://micro-manager.org/>) on a computer.

The microtubule flow field is estimated using PIV by analyzing the images at 660 nm. The PIV is performed by a custom code written in Matlab³⁵ to measure the velocity field of the microtubule contraction dynamics (within the illumination region) and microtubule movements alongside the fluid flow (outside the illumination region). In particular, the microtubule velocity field is determined through local maximization of the correlation between the warped and the target images.

For the simulation in Fig. 1f, g, active particles are modeled as point forces that generate two-dimensional Stokeslets²⁷. The force vectors point toward the center of

the contracting network with a magnitude that is proportional to the particle’s distance from the activation area center.

The flow field is measured by first comparing the position of individual inert particles from frame to frame³⁶ for the particle displacement with a nearest-neighbor algorithm (15 pixels threshold)³⁷. Then the displacement vector field, which is sparse due to the randomness of the particle locations, is grouped within a 30×30 pixels consecutive window and averaged over minute 2 to minute 15 of the experiment. The velocity field is calculated by dividing the displacement field by the time interval between frames, 5 s. Finally, the velocity field at each time step of the experiment is calculated and averaged to get the time-averaged velocity field.

The solution to Eq. (1) with the boundary conditions described in the text was found by employing FEM. In particular, the FeniCS library²⁶ was used in our code, which can be found on GitHub: <https://github.com/domischi/StokesFEM>. No-slip boundary conditions were applied at the upper and lower edge of the simulation cell, as well as in a central region with half the linear size of the activation region. The point forces were spread out over a small region, with one-tenth of the size of the activated region. The solution approach further used Taylor–Hoods basis functions and a quadratic meshing. Additional details can be found in Supplementary Methods 6.

Reporting summary. Further information on research design is available in the Nature Research Reporting Summary linked to this article.

Data availability

The data is openly available at <https://doi.org/10.22002/D1.1858>.

Code availability

The code to reproduce our main findings can be found on the following Github repositories: The FEM code can be found on <https://github.com/domischi/StokesFEM> and the PIV analysis code is on https://github.com/ShaiShdk/ActiveFlow_PIV.

Received: 3 April 2021; Accepted: 10 August 2021;

Published online: 27 August 2021

References

- Allen, N. S. & Allen, R. D. Cytoplasmic streaming in green plants. *Annu. Rev. Biophys. Bioeng.* **7**, 497–526 (1978).
- Behkam, B. & Sitti, M. Bacterial flagella-based propulsion and on/off motion control of microscale objects. *Appl. Phys. Lett.* **90**, 023902 (2007).
- Berg, H. C. & Anderson, R. A. Bacteria swim by rotating their flagellar filaments. *Nature* **245**, 380–382 (1973).
- Boon, R. A. & Vickers, K. C. Intercellular transport of microRNAs. *Arterioscler. Thromb. Vasc. Biol.* **33**, 186–192 (2013).
- Pierce-Shimomura, J. T. et al. Genetic analysis of crawling and swimming locomotory patterns in *C. elegans*. *Proc. Natl Acad. Sci. USA* **105**, 20982–20987 (2008).
- Videler, J. J. *Fish Swimming*. Vol. 10 (Springer Science & Business Media, 1993).
- Keren, K., Yam, P. T., Kinkhabwala, A., Mogilner, A. & Theriot, J. A. Intracellular fluid flow in rapidly moving cells. *Nat. Cell Biol.* **11**, 1219–1224 (2009).
- Monteith, C. E. et al. A mechanism for cytoplasmic streaming: kinesin-driven alignment of microtubules and fast fluid flows. *Biophys. J.* **110**, 2053–2065 (2016).
- Batchelor, C. K. & Batchelor, G. *An Introduction to Fluid Dynamics* (Cambridge University Press, 2000).
- Wu, K.-T. et al. Transition from turbulent to coherent flows in confined three-dimensional active fluids. *Science* **355**, eaal1979 (2017).
- Woodhouse, F. G. & Goldstein, R. E. Spontaneous circulation of confined active suspensions. *Phys. Rev. Lett.* **109**, 168105 (2012).
- Hentrich, C. & Surrey, T. Microtubule organization by the antagonistic mitotic motors kinesin-5 and kinesin-14. *J. Cell Biol.* **189**, 465–480 (2010).
- Urrutia, R., McNiven, M. A., Albanesi, J. P., Murphy, D. B. & Kachar, B. Purified kinesin promotes vesicle motility and induces active sliding between microtubules in vitro. *Proc. Natl Acad. Sci. USA* **88**, 6701–6705 (1991).
- Nédélec, F., Surrey, T., Maggs, A. C. & Leibler, S. Self-organization of microtubules and motors. *Nature* **389**, 305 (1997).
- Sanchez, T., Chen, D. T., DeCamp, S. J., Heymann, M. & Dogic, Z. Spontaneous motion in hierarchically assembled active matter. *Nature* **491**, 431–434 (2012).
- Guillamat, P., Ignés-Mullol, J. & Sagués, F. Taming active turbulence with patterned soft interfaces. *Nat. Commun.* **8**, 1–8 (2017).
- Opathalage, A. et al. Self-organized dynamics and the transition to turbulence of confined active nematics. *Proc. Natl Acad. Sci. USA* **116**, 4788–4797 (2019).

18. Hitt, A., Cross, A. & Williams, R. Microtubule solutions display nematic liquid crystalline structure. *J. Biol. Chem.* **265**, 1639–1647 (1990).
19. Ross, T. D. et al. Controlling organization and forces in active matter through optically defined boundaries. *Nature* **572**, 224–229 (2019).
20. Foster, P. J., Fürthauer, S., Shelley, M. J. & Needleman, D. J. Active contraction of microtubule networks. *Elife* **4**, e10837 (2015).
21. Schildknecht, D. & Thomson, M. Phenomenological model of motility by spatiotemporal modulation of active interactions. *New J. Phys.* **23**, 083001 (2021).
22. Mogilner, A. & Manhart, A. Intracellular fluid mechanics: coupling cytoplasmic flow with active cytoskeletal gel. *Annu. Rev. Fluid Mech.* **50**, 347–370 (2018).
23. Needleman, D. & Shelley, M. The stormy fluid dynamics of the living cell. *Phys. Today* **72**, 32–38 (2019).
24. Chwang, A. T. & Wu, T. Y. T. Hydromechanics of low-Reynolds-number flow. Part 2. Singularity method for Stokes flows. *J. Fluid Mech.* **67**, 787–815 (1975).
25. Blake, J. R. A note on the image system for a stokeslet in a no-slip boundary. *Math. Proc. Camb. Philos. Soc.* **70**, 303–310 (1971).
26. Alnaes, M. S. et al. The FEniCS Project Version 1.5. *Arch. Numer. Softw.* **3**, 9–23 (2015).
27. Spagnolie, S. E. & Lauga, E. Hydrodynamics of self-propulsion near a boundary: predictions and accuracy of far-field approximations. *J. Fluid Mech.* **700**, 105–147 (2012).
28. Howard, S. J., Oliveira, M. S., Alves, M. A. & McKinley, G. H. Optimized cross-slot flow geometry for microfluidic extensional rheometry. *Phys. Rev. Lett.* **109**, 128301 (2012).
29. Doostmohammadi, A., Ignés-Mullol, J., Yeomans, J. M. & Sagués, F. Active nematics. *Nat. Commun.* **9**, 3246 (2018).
30. Alim, K., Amselem, G., Peaudcerf, F., Brenner, M. P. & Pringle, A. Random network peristalsis in physarum polycephalum organizes fluid flows across an individual. *Proc. Natl Acad. Sci. USA* **110**, 13306–13311 (2013).
31. Sokolov, A., Apodaca, M. M., Grzybowski, B. A. & Aranson, I. S. Swimming bacteria power microscopic gears. *Proc. Natl Acad. Sci. USA* **107**, 969–974 (2010).
32. Vizsnyiczai, G. et al. Light controlled 3d micromotors powered by bacteria. *Nat. Commun.* **8**, 1–7 (2017).
33. Needleman, D. & Dogic, Z. Active matter at the interface between materials science and cell biology. *Nat. Rev. Mater.* **2**, 1–14 (2017).
34. Lau, A. W. C., Prasad, A. & Dogic, Z. Condensation of isolated semi-flexible filaments driven by depletion interactions. *Europhys. Lett.* **87**, 48006 (2009).
35. MATLAB. *Version 9.6 (R2019a)*. (The MathWorks Inc., Natick, Massachusetts, 2019).
36. Adamczyk, A. & Rimai, L. 2-dimensional particle tracking velocimetry (ptv): technique and image processing algorithms. *Exp. Fluids* **6**, 373–380 (1988).
37. Schmidt, T., Schütz, G., Baumgartner, W., Gruber, H. & Schindler, H. Imaging of single molecule diffusion. *Proc. Natl Acad. Sci. USA* **93**, 2926–2929 (1996).

Acknowledgements

We acknowledge funding from the Donna and Benjamin M. Rosen Bioengineering Center, Foundational Questions Institute and Fetzer Franklin Fund (through FQXi 1816), The Moore Foundation, The Packard Foundation, and Heritage Medical Research Institute. We thank Inna-Marie Strazhnik for the preparation of figures and illustrations. We acknowledge Dr. Guy Riddihough for his editorial assistance with the paper.

Author contributions

Z.Q., J.J., H.J.L., R.P., and M.T. conceived the project. Z.Q., H.J.L., D.L., and F.Y. performed the experiments. J.J. performed the initial investigations of the model. D.S. developed the theoretical framework and performed the finite-element simulations. S.S. performed the PIV analysis. E.A. performed the image segmentation analysis. Z.Q., D.S., and M.T. wrote the paper with input from all authors.

Competing interests

The authors declare no competing interests.

Additional information

Supplementary information The online version contains supplementary material available at <https://doi.org/10.1038/s42005-021-00703-3>.

Correspondence and requests for materials should be addressed to Z.Q., D.S. or M.T.

Peer review information *Communications Physics* thanks the anonymous reviewers for their contribution to the peer review of this work.

Reprints and permission information is available at <http://www.nature.com/reprints>

Publisher's note Springer Nature remains neutral with regard to jurisdictional claims in published maps and institutional affiliations.



Open Access This article is licensed under a Creative Commons Attribution 4.0 International License, which permits use, sharing, adaptation, distribution and reproduction in any medium or format, as long as you give appropriate credit to the original author(s) and the source, provide a link to the Creative Commons license, and indicate if changes were made. The images or other third party material in this article are included in the article's Creative Commons license, unless indicated otherwise in a credit line to the material. If material is not included in the article's Creative Commons license and your intended use is not permitted by statutory regulation or exceeds the permitted use, you will need to obtain permission directly from the copyright holder. To view a copy of this license, visit <http://creativecommons.org/licenses/by/4.0/>.

© The Author(s) 2021